Journal of Solid State Electrochemistry
https://doi.org/10.1007/s10008-017-3859-x

ORIGINAL PAPER

On the effect of the carbonaceous substrate in the nucleation of Sn nanoparticles for Li-ion anodes: experiments and first principles calculations

Sacha Smrekar[1,4] · Martin E. Zoloff Michoff[2] · Jorge E. Thomas[3] · Cecilia A. Calderón[1,4] · Lucas M. Farigliano[2] · Arnaldo Visintin[3] · Ezequiel P. M. Leiva[2] · Daniel E. Barraco[1,4]

Received: 20 September 2017 / Revised: 17 November 2017 / Accepted: 6 December 2017

Abstract
The nucleation of Sn nanoparticles by chemical reduction was studied using three different carbonaceous substrates, to obtain Sn/C composites. When used as active materials in anodes for lithium-ion batteries, these composites displayed higher capacities than commercially used graphite, and showed a good cyclability. The differences in morphology, capacity, cyclability, and diffusion between the resulting materials are highlighted. The resulting materials were characterized by charge-discharge cycling, voltammetry, EIS, SEM, and TEM microscopy. It was found that the substrate has a determinant effect on the deposition of Sn. This effect is interpreted in terms of the relative adsorption energies of a single Sn atom obtained from DFT calculations.

Keywords Li-ion batteries · Sn · Carbon-based materials · DFT

Introduction

Among the materials proposed as anodes for the next generation lithium-ion batteries, there has been a great interest in tin and its composites. Tin has a higher capacity (for example, 998 mAh/g for $SnLi_{4.4}$ [1]) than the commercially used graphite (372 mAh/g) and it shows several industrial advantages. It has relatively simple and scalable synthesis routes, and either its oxides or its metallic form can be used as anodes. However, in order to apply Sn-based anodes to batteries, there are still some technical difficulties to overcome. One of them is the large volume change that occurs during the charging/discharging processes which leads to poor cyclability, mechanical failure of the material, and loss of electrical contact [2]. Current research has been focused on solving these issues, and several strategies for achieving this goal have been proposed [3]. One of these is the combination of Sn with other materials capable of containing the volume change without losing the electrical contact, graphite being the natural candidate for this role. In 2004, Wang et al. [4] synthesized Sn nanoparticles on synthetic graphite using $SnCl_4$ and $NaBH_4$ as reducing agent, achieving capacities slightly higher than graphite for 60 cycles. At the same time, Trifonova et al. [5] observed that $NaBH_4$ was a good reducing agent for the synthesis of Sn/Sb alloys as anode materials. In 2009, this method was applied to graphene nanosheets by Yao et al. [6] and a substantial improvement in capacity and cyclability was observed. Recently [7], it was reported that

Electronic supplementary material The online version of this article (https://doi.org/10.1007/s10008-017-3859-x) contains supplementary material, which is available to authorized users.

✉ Sacha Smrekar
sachasmrekar@gmail.com

✉ Martin E. Zoloff Michoff
martin.zoloff@unc.edu.ar

[1] Instituto de Física Enrique Gaviola (IFEG), CONICET, Ciudad Universitaria, 5000 Córdoba, Argentina

[2] INFIQC, CONICET and Departamento de Química Teórica y Computacional, Facultad de Ciencias Químicas, Universidad Nacional de Córdoba, Ciudad Universitaria, 5000 Córdoba, Argentina

[3] Instituto de Investigaciones Fisicoquímicas Teóricas y Aplicadas (INIFTA), Facultad de Ciencias Exactas, Universidad Nacional de La Plata, CCT La Plata-CONICET, C.C. 16, Suc. 4, 1900 La Plata, Argentina

[4] Facultad de Matemática, Astronomía, Física y Computación, Universidad Nacional de Córdoba, Córdoba, Argentina

Published online: 11 January 2018

carbon-coated graphite particles show enhanced adhesion of Sn nanoparticles, thus increasing their cyclability as electrodes. Yet, to the best of our knowledge, neither a systematic study has been made about the influence of the carbonaceous substrate on the synthesis of active materials by reduction of Sn with $NaBH_4$, nor a consistent explanation for this type of phenomena has been sought in terms of first principles calculations.

In the present study, Sn-based carbonaceous materials were synthesized by simple chemical reduction of $SnCl_2$ over different carbonaceous materials (amorphous carbon, graphite, and multi-walled carbon nanotubes). The resulting materials were characterized chemically and physically, and their electrochemical performance as anodes for lithium-ion secondary batteries was studied using various analytical techniques. The results obtained are analyzed comparatively in order to determine the best substrate for synthesizing anodic materials employing this method. Density Functional Theory (DFT) calculations were carried out in order to rationalize the observed experimental trends. The adsorption energy of a single Sn atom, which can be used as a reference regarding the thermodynamic driving force for Sn nucleation, turned out to be the key factor to understand the differences between the various carbonaceous materials studied.

Experimental section

Sn/C composite synthesis

0.025 mol of anhydrous $SnCl_2$ were dissolved in 150 mL of ethyleneglicol, then, under constant stirring, 1.5 g of the carbonaceous support and 0.3 g of polyvinylpyrrolidone (PVP) were added to the solution (approximately 30 and 5 wt%, respectively). When the dispersion became homogeneously mixed, 0.025 mol of $NaBH_4$ were slowly added to ensure the total reduction of $SnCl_2$, under stirring at room temperature. This methodology is similar to that used to prepare tin nanoparticles [8] or tin-alloyed nanoparticles [9] in a homogeneous nucleation and growth process. Thus, the reduction process of Sn ions provided from the precursor may be represented by the following reaction [8]:

$$BH_4^- + 8OH^- + 4Sn^{2+} \rightarrow B(OH)_4^- + 4H_2O + 4Sn$$

After adding the reducing agent, the samples were stirred during 1 h. Although we have not done a study of the kinetics of the chemical reduction process, this has been performed in the case of the synthesis of Sn-3.5 Ag-0.5 Cu nanoparticles by reduction $NaBH_4$ [9]. In the aforementioned work, it was shown that the particle size increases rapidly during the initial 60 s and afterwards, the growth is much slower. Therefore, we could safely assume that after 1 h of reaction, the growth process of Sn/C nanoparticles has reached a steady state situation. Thereafter, the mixtures were filtered and carefully washed with fresh ethyleneglicol and miliQ water several times. The resulting materials were dried in an oven at 80 °C for 24 h, ground and sieved. It is likely that at this stage, some SnO_2 is formed on the surface of the tin nanoparticles by oxidation from the ambient oxygen. Although the extent of oxide formation has not been quantified here, according to the literature, its content should not be higher than ca. 5 wt%. [10]. Three different carbon materials were used as support: amorphous carbon (Super P®) from Timcal-Imerys, commercial graphite flakes from Sigma-Aldrich, and multi-walled carbon nanotubes (100 nm diameter) from Sigma-Aldrich. These samples were named Sn-BH-SP, Sn-BH-G, Sn-BH-NT, respectively. Less than 3 g of the Sn/C composites were obtained per batch. It must be noted that it was not possible to calculate the chemical yield because during the filtration procedure, a small part of the samples was always glued to the membrane and this fraction was discarded to avoid contamination problems.

Physical characterization

All the obtained materials were characterized by BET analysis, Transmission (TEM) and Scanning (SEM) Electron Microscopy, and, also, by Energy Dispersive Scanning (EDS).

Electrochemical characterization

All the procedures outlined were conducted in a dry argon environment. The electrochemical properties of the synthesized anodes used in the rechargeable lithium-ion batteries experiments were determined in a controlled room temperature at 25 °C. The working electrode consisted of 80 wt% of the active material (Sn/C composite), 10 wt% of a conductive carbon additive (Super P®), and 10 wt% of PVDF binder. A lithium foil was used as the counter and as reference electrodes in a Swagelok type cell in a three-electrode array. All potentials reported here refer to the Li^+/Li^0 redox potential. The electrolyte was 1 M $LiPF_6$ in a 1:1 wt/wt mixture of ethyl carbonate (EC): dimethyl carbonate (DMC). Cell assembly was carried out in a MBraun glove box with the concentrations of moisture and oxygen below 1 ppm. The geometric areas of the electrodes were 1.2 cm^2 (diameter 12.4 mm) with an average of 1 mg of active material per electrode and 20 μm of active layer thickness. All the informed capacities were calculated taking into account the mass of the active material (Sn/C composite). The C rates were calculated as the function of the maximum measured capacity of each electrode, where 1 C means the necessary current to charge (or discharge) the electrode in 1 h. The cycling performance of the electrodes was studied using a Multichannel Arbin BT-2000 test station, and details concerning the electrode preparation and cell

assembly can be found elsewhere [11, 12]. Cells were charged and discharged at a constant current of C/2 for 20 cycles, with the fixed voltage limits being between 0.01 and 1.50 V. Cyclic voltammetry (CV) and electrochemical impedance spectroscopy (EIS) were performed on an Autolab PGSTAT302N potentiostat. After the first cycling, the experiment was paused for CV and EIS characterization. Cyclic voltammetries were carried out between 0.01 and 3.00 V, with scan rates of 2, 1, 0.5, and 0.1 mV/s. The EIS test was performed at discharged states (or delithiated), using a potentiostatic method at the open-circuit potential (OCP), with 10 mV amplitude and frequencies ranging from 100 kHz to 5 mHz. After CV and EIS characterization, the cells were cycled for another 80 cycles at a current of 1 C.

Model and computations

All calculations were performed using the Quantum Espresso package [13] within the PBE [14]/PAW framework of Density Functional Theory (DFT). A plane-wave energy cutoff of 45 Ry (ca. 612 eV) was used throughout with an electronic density energy cutoff of 270 Ry (ca. 3673 eV). Geometry optimization of all atoms and cell parameters was performed employing the Broyden-Fletcher-Goldfarb-Shanno (BFGS) algorithm. Spin-polarization was considered in all calculations. Van der Waals interactions were taken into account using the DFT-D method.

Adsorption energies of Sn atoms on different carbon-based materials were calculated as given in Eq. (1):

$$E_{\mathrm{ad}} = E(\mathrm{Sn/C}) - E(\mathrm{Sn}_{bulk}) - E(\mathrm{C}) \quad (1)$$

where E(Sn/C) is the energy of the optimized structure of the corresponding adsorbates, $E(\mathrm{Sn_{bulk}})$ is the energy for bulk α-Sn, and E(C) is the energy of the carbonaceous material.

Three different carbon materials were modeled: (1) A graphene layer was used to emulate the surface of large diameter carbon nanotubes (NT), as the ones used in the present experiments. Graphene nanoribbons (NR) were employed to emulate the edge of these large carbon nanotubes. (2) Bulk graphite and a stack of graphene nanoribbons (GNR) were used to emulate adsorption between the graphite sheets and on the edge of steps in graphite, respectively. (3) A surface of an amorphous carbon structure with a density of ca. 2.0 g/cm^3 was used to emulate the adsorption of Sn on carbon Super P®, as used in experiments.

Although oxygen functionalities (e.g., C=O, C–OH, C–OOH) are usually present on the surface of carbonaceous materials, under the strongly reducing conditions used to synthesize the Sn/C composites, it can be safely assumed that these types of functionalities are effectively reduced. For instance, graphene oxide is electrochemically reduced at − 0.75 V vs. reversible hydrogen electrode [15], whereas the reduction potential of $NaBH_4$ is − 1.24 V (vs. SHE), i.e., ca. 2-times larger than the threshold potential required to reduce oxygenated functionalities on a graphene sheet. In fact, it has been shown that graphite oxide is efficiently reduced by 50–150 mM aqueous solutions of $NaBH_4$ [16]. Thus, oxygen functionalities have not been considered in our models for the carbon support materials.

Surface calculations were done using a 32 carbon-atom layer. Vacuum of 10 Å in the direction perpendicular to the surface was used to avoid spurious interactions between the periodic images. In this case, the Brillouin zone was sampled in a 5 × 5 × 1 irreducible Monkhorst-Pack [17] *k*-point grid. A pristine surface (Graphene-*pr*), as well as a Stone-Wells (Graphene-*SW*) and a single vacancy (Graphene-*sv*) defects were considered.

Graphene nanoribbons with either zigzag or armchair edges were also considered. In these cases, a 15 Å vacuum was employed in the direction orthogonal to the edge and a 5 × 1 × 1 *k*-point grid was used.

Bulk calculations were carried out using four layers of AB graphite containing a total of 128 carbon atoms. For these calculations a 5 × 5 × 5 *k*-point grid was used. Pristine graphite (Graphite-*pr*) and a defective one with a single vacancy in one of the layers (Graphite-*sv*) were considered. Calculations for a stack to four GNRs in an AB geometry exposing the armchair edge were performed using a 5 × 5 × 1 *k*-point grid and 15 Å vacuum in the direction orthogonal to the edge.

For the case of the calculations involving the adsorption of Sn atoms on the edges of a single GNR or the stack of four graphene NRs in AB geometry, Sn atoms were placed symmetrically on both edges exposed to the vacuum. In these cases, the adsorption energy was computed according to Eq. (2):

$$E_{\mathrm{ad}} = E(\mathrm{Sn–C}) - 2E(\mathrm{Sn}_{bulk}) - E(\mathrm{C}) \quad (2)$$

Amorphous carbon was obtained by melting and freezing a diamond structure using molecular dynamics. First, carbon atoms were randomly removed from a cubic diamond supercell of 10.7 Å by side to give the desired density of ca. 2.0 g/cm^3. Two different initial structures, say A and B containing 123 atoms each, were produced by removing a different set of carbon atoms. Each of these was subject to a temperature ramp until a temperature of 3000 K was reached. Afterwards, temperature was decreased until ca. 100 K and the resulting structures were optimized using the conjugate gradients algorithm. Molecular dynamics was carried out using LAMMPS [18] and interatomic interactions were described according to the reactive force-field ReaxFF [19]. The resulting amorphous structures of carbon atoms were further optimized with DFT. Radial distribution functions and relative distribution of single-, bi-, tri-, and tetra-coordinated carbon atoms very similar to other structures reported in the literature [20, 21] were obtained. The resulting bulk materials

obtained, A and B, are structurally very similar and represent two different local minimum structures. Each of these was cleaved in half to give amorphous carbon surfaces, containing 60–64 atoms each. One of these halves for each amorphous carbon structure was chosen and re-optimized. Sn atoms were positioned in the vicinity of low-coordinated carbon atoms and the system was optimized. In these cases, the carbon atoms within 1.5 Å from the bottom of the slab were kept fixed in their positions. A vacuum layer of 10 Å and a 5 × 5 × 1 *k*-point grid were employed.

Results and discussion

Physical characterization

All the samples were studied by scanning electron microscopy. The morphology of Sn-BH-SP at micro and nanoscale are shown in Fig. 1a and Fig. 2a, respectively, where it can be observed that the material exhibits an irregular porous surface with no clear phase separation. The EDS scan, shown in Fig. 3a, revealed a uniform presence of Sn over the whole surface, and thus, there were no localized agglomerates of pure Sn.

The sample Sn-BH-G, for which SEM micrographies are shown in Figs. 1b and 2b, manifests the occurrence of relatively large Sn clusters on the surface of graphite. The EDS scan for this sample is illustrated in Fig. 3b. The large dimensions of these Sn agglomerates are expected to be disadvantageous for lithium-ion storage under electrochemical cycling. The successive changes of volume would likely result in material fracture to generate much smaller particles, thus losing electrical contact with the carbon support, which works as current collector. The direct consequence of this phenomenon is expected to be a pronounced loss of capacity for this material.

SEM images of sample Sn-BH-NT are shown in Figs. 1c and 2c, where the expected morphology of the carbon nanotubes decorated with small particles can be observed. The EDS scan, in Fig. 3c, shows a uniform distribution of particles without Sn agglomeration, similar to that of the sample of Sn-BH-SP. For all the synthesized samples, an average Sn content of 17 wt% was determined by the semi-quantitative EDS analysis.

In the TEM micrographies of the samples, shown in Fig. 4, it can be seen that the adsorbed Sn forms nanoparticles of approximately 10 nm in diameter. It should be noted that the degree of aggregation varied remarkably. In the sample Sn-BH-SP, the nanoparticles were much more dispersed than in the others, a feature which is expected to be beneficial for the performance of the electrode.

The influence of the nature of the carbonaceous substrate on the way in which the particles are deposited has been shown for other systems, also synthesized using a metal reduction procedure [22]. It was demonstrated that several factors, such as the amount and type of surface imperfections, may influence the adsorption process [22]. Consequently, for the deposition observed in our materials, the selected carbon supports were not only different in morphology (amorphous, crystalline, and

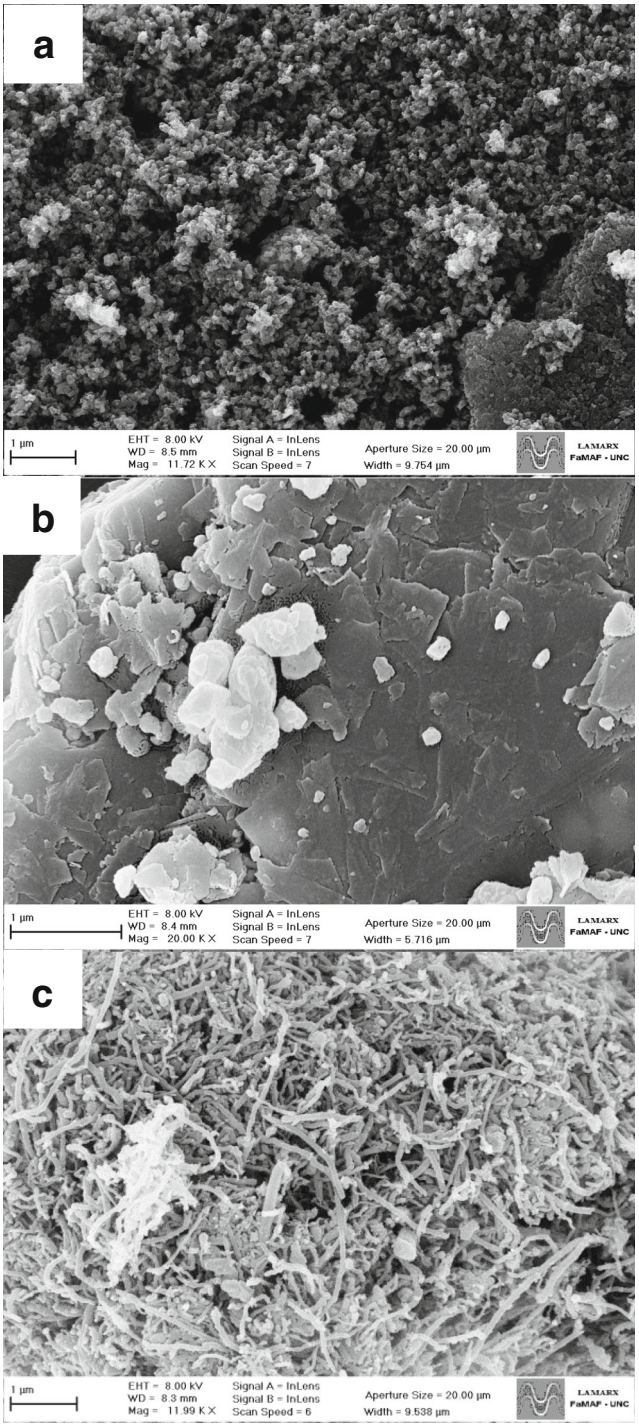

Fig. 1 SEM images at the microscale for **a** Sn-BH-SP, **b** Sn-BH-G, and **c** Sn-BH-NT

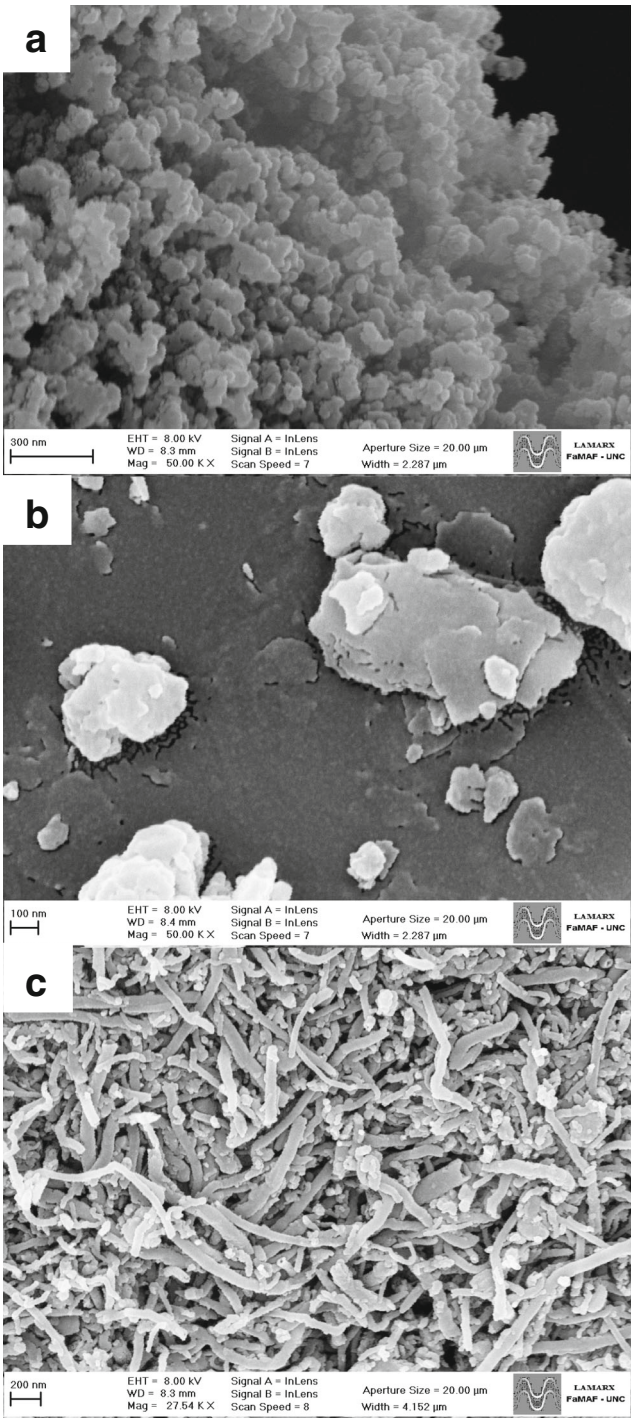

Fig. 2 SEM images at the nanoscale for **a** Sn-BH-SP, **b** Sn-BH-G, and **c** Sn-BH-NT

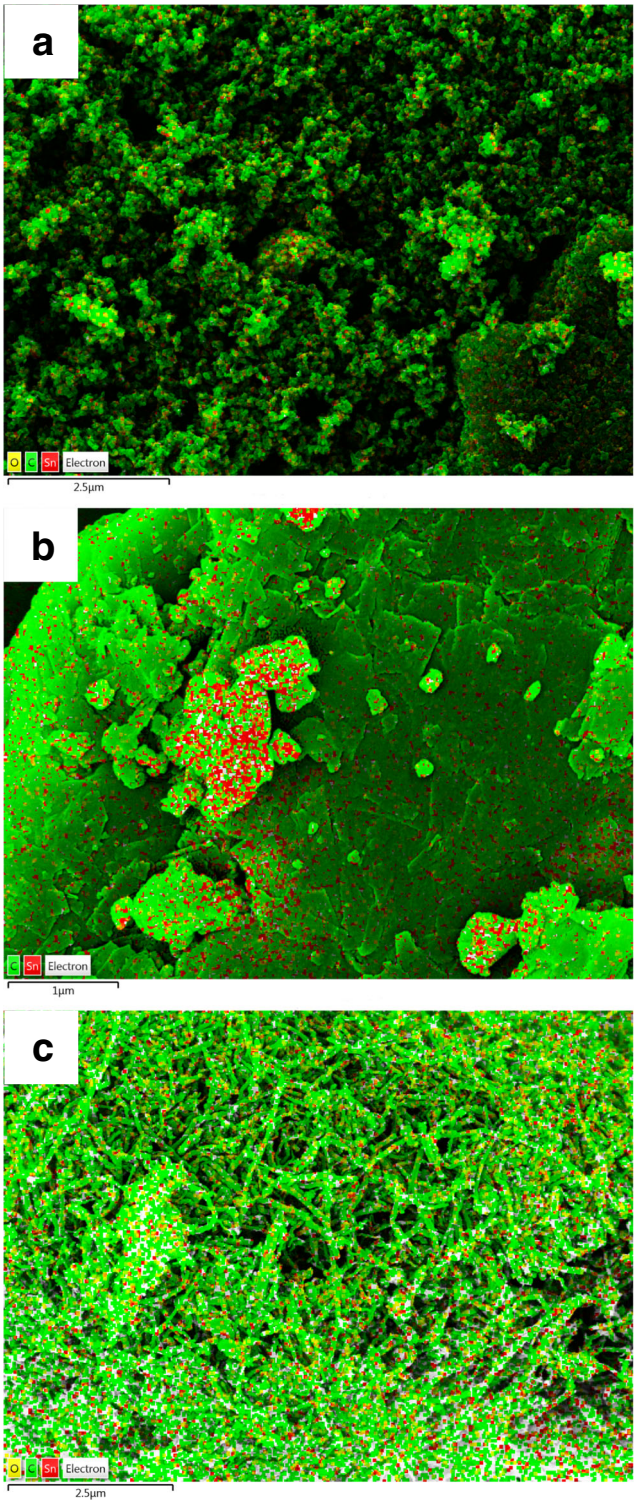

Fig. 3 EDS mappings for **a** Sn-BH-SP, **b** Sn-BH-G, and **c** Sn-BH-NT. Green represents carbon and red represents Sn

nanostructured), but also had large variations in specific area and number of imperfections. For instance, in the case of nanotubes, acid groups were sometimes found on the surface after the purification process.

The carbon samples and the Sn/C composites were characterized by BET analysis. The obtained specific surfaces for the carbon support materials were 61 m^2/g for amorphous carbon, 2 m^2/g for the graphite flakes, and 72 m^2/g for the carbon nanotubes. For the different Sn/C composites, the final specific areas obtained were 54 m^2/g for Sn-BH-SP, below the detection limit for Sn-BH-G and

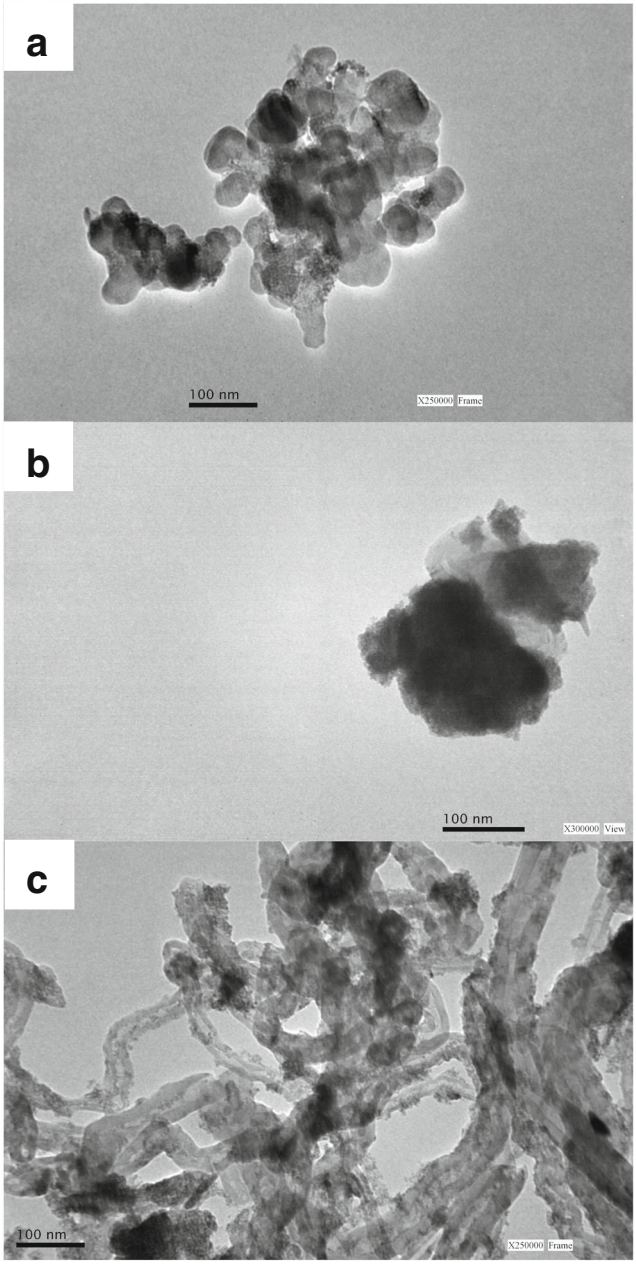

Fig. 4 TEM micrographies for **a** Sn-BH-SP, **b** Sn-BH-G, and **c** Sn-BH-NT

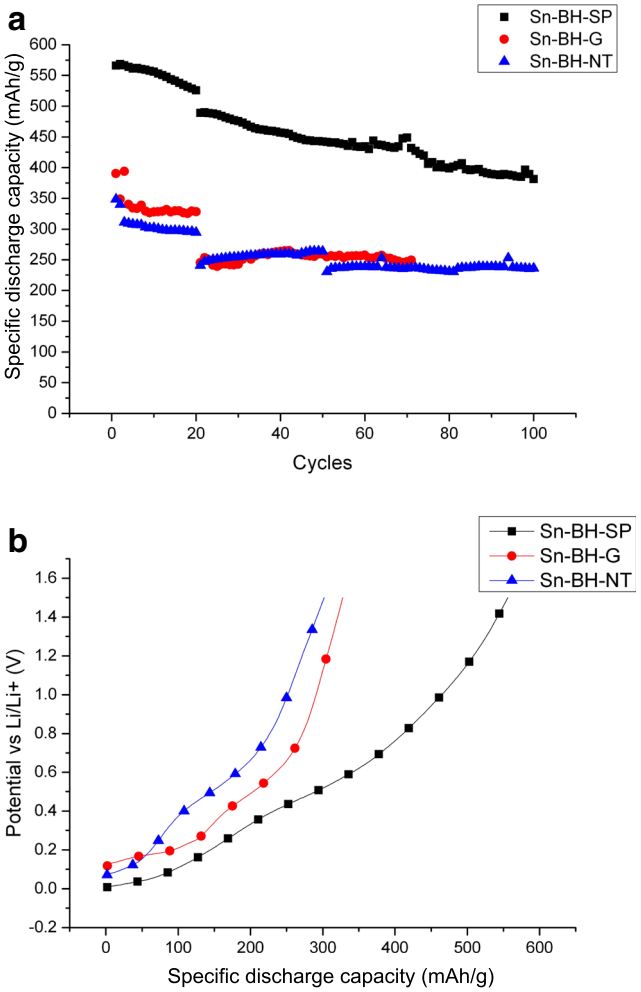

Fig. 5 **a** Specific discharge capacity vs. number of cycles, and **b** discharge profile at 1 C

65 m^2/g for Sn-BH-NT. The BET isotherms are illustrated in Fig. S1 in the Supplementary Material provided.

Electrochemical results

Charge and discharge cycles

Figure 5a shows the performance of the cells over the whole cycling process. These results demonstrate that the electrode made of Sn-BH-SP has a superior specific charge capacity (566 mAh/g) in the first cycle, compared with the electrodes made of Sn-BH-G and Sn-BH-NT, which had specific capacities of 425 and 349 mAh/g, respectively. The Sn-BH-SP electrodes had also the highest capacity retention after 20 cycles at C/2, retaining 92.9% of their initial capacity, while Sn-BH-G and Sn-BH-NT only retained 83.7 and 84.4% of their initial capacities, respectively. At this point, voltammetry and EIS analysis were performed on the cells. Thereafter, cycling was resumed at 1C and continued up to 100 cycles (70 in the case of Sn-BH-G). The differences in capacity found before and after the voltammetries (cycles 20th to 30th) can be explained by taking into account that the cycling current density was changed in order to obtain more cycles in a reasonable time. The final capacities of the samples, after this cycling process, were 381 mAh/g for Sn-BH-SP, 249 mAh/g for Sn-BH-G, and 235 mAh/g for Sn-BH-NT.

Figure 5b shows the discharge profiles at 1 C of the synthesized materials. Due to the nature of the lithiation process of Sn (lithium alloying), these discharges do not show the typical plateau that is usually observed for materials with lithium intercalation [23]. However, the

discharge potentials (at 50% of SOC) are around 0.5 V for all the Sn/C materials. These potentials decrease at lower C rates, as it is possible to see in Fig. S2 in the Supplementary Material provided. The coulombic efficiency of the Sn/C composites studied here was very good up to ca. 100 cycles (refer to Fig. S3 in the Supplementary Material provided).

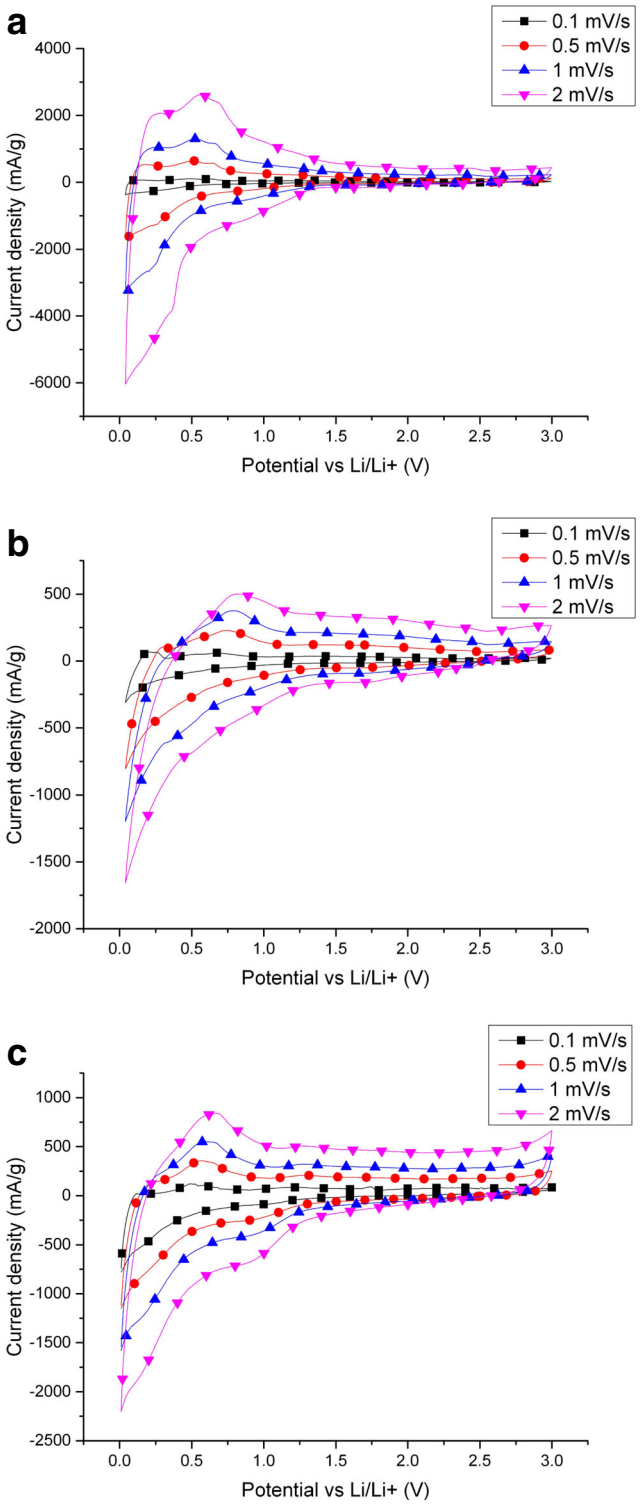

Fig. 6 Voltammograms of **a** Sn-BH-SP, **b** Sn-BH-G, and **c** Sn-BH-NT at different scan rates

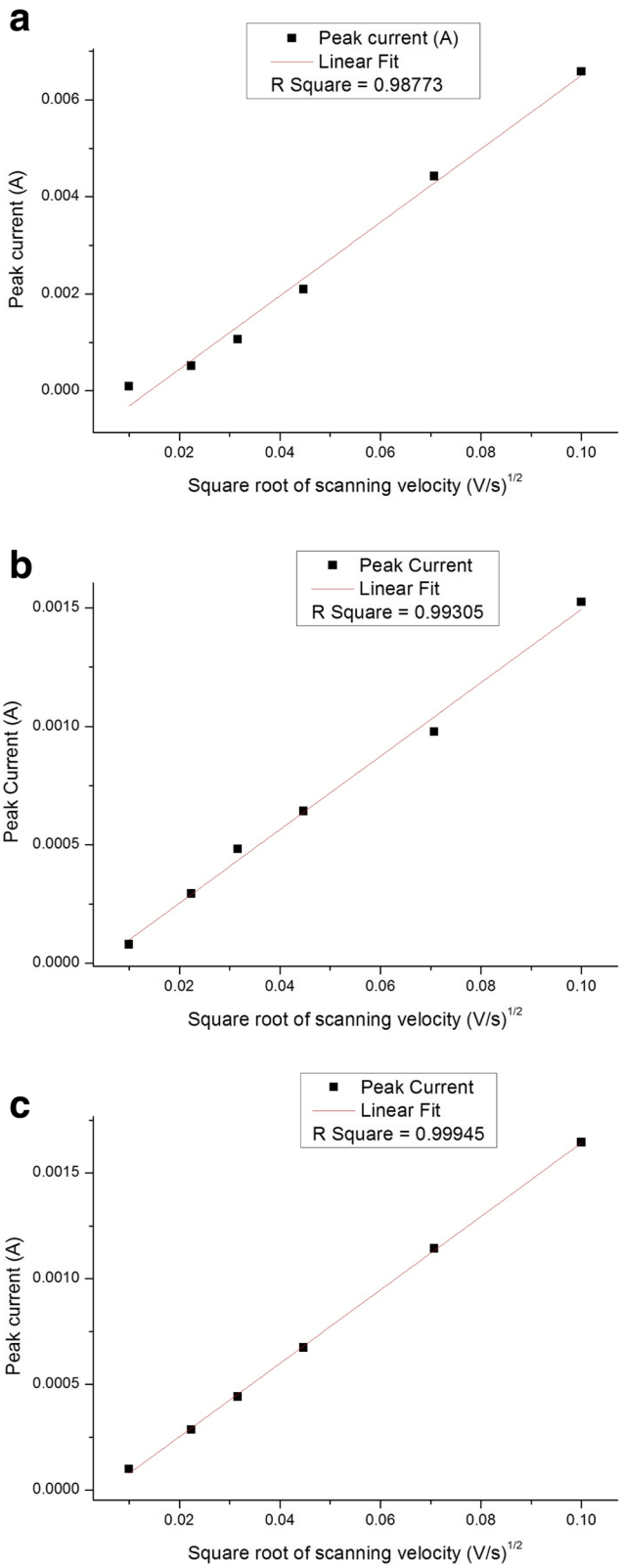

Fig. 7 Linear fit of the current density peak vs. (scanning rate)$^{1/2}$ for **a** Sn-BH-SP, **b** Sn-BH-G, and **c** Sn-BH-NT

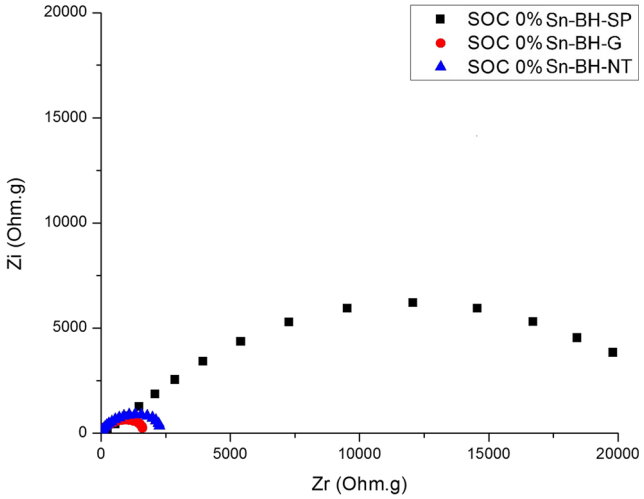

Fig. 8 Nyquist diagrams from EIS response at 0% of SOC for Sn-BH-SP, Sn-BH-G, and Sn-BH-NT

Cyclic voltammetry

Cyclic voltammograms at different scan rates of the materials are shown in Fig. 6. It can be seen that the main anodic peaks, corresponding to the delithiation processes of the samples, are in the potential window between 0.5 and 0.8 V. This potential is closer to the delithiation potential of graphite than to that of other anodic materials such as lithium titanates [24].

From the voltammograms, it can be seen that the current peak increased with a rise in scan rate. A linear fit of the data revealed that the growth of the peak current was proportional to the square of the scan rate (see Fig. 7). Although the system is not fully reversible, and Randles-Sevcik equation cannot be strictly applied, this correlation helps to give us a better insight into the diffusional behavior of the materials using an apparent diffusion coefficient [25]. The Randles-Sevcik, Eq. (3), (at 25 °C) states that

$$i_p = 268600\, n^{3/2} A C D^{1/2} v^{1/2} \quad (3)$$

where i_p is the peak current [A], n is the transference number, A is the electrode's area [cm^2], C is the concentration of lithium in the electroactive material [mol/cm^3], D is the diffusion coefficient [cm^2/s], and v is the scan rate [V/s]. This equation can also be rewritten to determine an apparent value that includes the diffusion in the composite and the transference on the electrolyte. In this way, the apparent diffusion coefficient can be obtained [25], according to Eq. (4)

$$i_p \cdot m^{-1} = 268600\, n^{3/2} A_e C D_{app}{}^{1/2} v^{1/2} \quad (4)$$

with m being the mass of the electrode, and A_e the specific area per unit of mass. The transference number for the lithiation and delithiation of the material is 1. Taking into account that the density of the phase with highest lithiation degree, $Li_{22}Sn_5$, is 2.56 g/cm^3, and that the molecular weight of the compound is 746.18 g/mol, then it follows that the maximum concentration of Li in the anode is 0.018 mol/cm^3. Being a porous material, the calculated active area per unit of mass was ca. 0.2 m^2/g for all the samples. These values were obtained by electrochemical impedance spectroscopy (EIS), fitting the intermediate frequencies with a simple R (R, CPE) circuit. EIS spectra for the samples studied here are illustrated in Fig. 8. From the EIS results, it is possible to notice that charge transfer resistance values have the following trend: graphite presents the lower resistance values, followed by carbon nanotubes, and then amorphous carbon. This trend can be attributed to the degree disorder of the carbon samples, which increases in the same direction. It is also well known that ordered graphitized structures are better electrical conductors than amorphous carbon materials, which can be conductive but not as good as

Table 1 Apparent diffusion coefficients from cyclic voltammetry and EIS results

Sample	Linear fit slope, $As^{1/2}V^{1/2}$	Apparent diffusion coefficient, $\times 10^{-12}$ cm^2/s
Sn-BH-SP	75.70	61.2
Sn-BH-G	13.83	2.04
Sn-BH-NT	17.39	3.23

Table 2 Adsorption energies (E_{ad}) for the systems studied, calculated according to Eqs. (1) and (2) and Bader charges for the Sn atom and the carbon material for each adsorbate structure. The denomination of A, B, A-1, A-2, B1, and B2 correlates with that used in Figs. 9, 10, and 11

System		E_{ad}, eV	Bader charges, e	
			Sn[a)]	C[b)]
Graphene-*pr*		+ 2.76	+ 0.30	− 0.30
Graphene-*SW*		+ 2.00	+ 0.65	− 0.65
Graphene-*sv*		− 1.07	+ 0.88	− 0.88
GNR-armchair	A	− 0.29	+ 0.88[c)]	− 1.76
	B	− 0.28	+ 0.79[c)]	− 1.58
GNR-zigzag	A	− 1.78	+ 0.87[c)]	− 1.74
	B	− 0.85	+ 0.84[c)]	− 1.68
Graphite-*pr*		+ 4.09	+ 0.82	− 0.82
Graphite-*sv*		+ 0.25	+ 0.99	− 0.99
Graphite-armchair	A	− 0.62	+ 0.95[c)]	− 1.90
	B	− 0.51	+ 0.98[c)]	− 1.96
	C	− 0.66	+ 0.85[c)]	− 1.70
	D	− 0.86	+ 0.90[c)]	− 1.80
Amorphous C	A-1	− 0.36	+ 0.87	− 0.87
	A-2	− 0.12	+ 0.88	− 0.88
	B-1	− 1.19	+ 0.93	− 0.93
	B-2	− 1.38	+ 1.01	− 1.01

[a)] Bader charge for each Sn atom in the supercell

[b)] Average Bader charge for the C atoms

[c)] Average for the 2 Sn atoms in the supercell

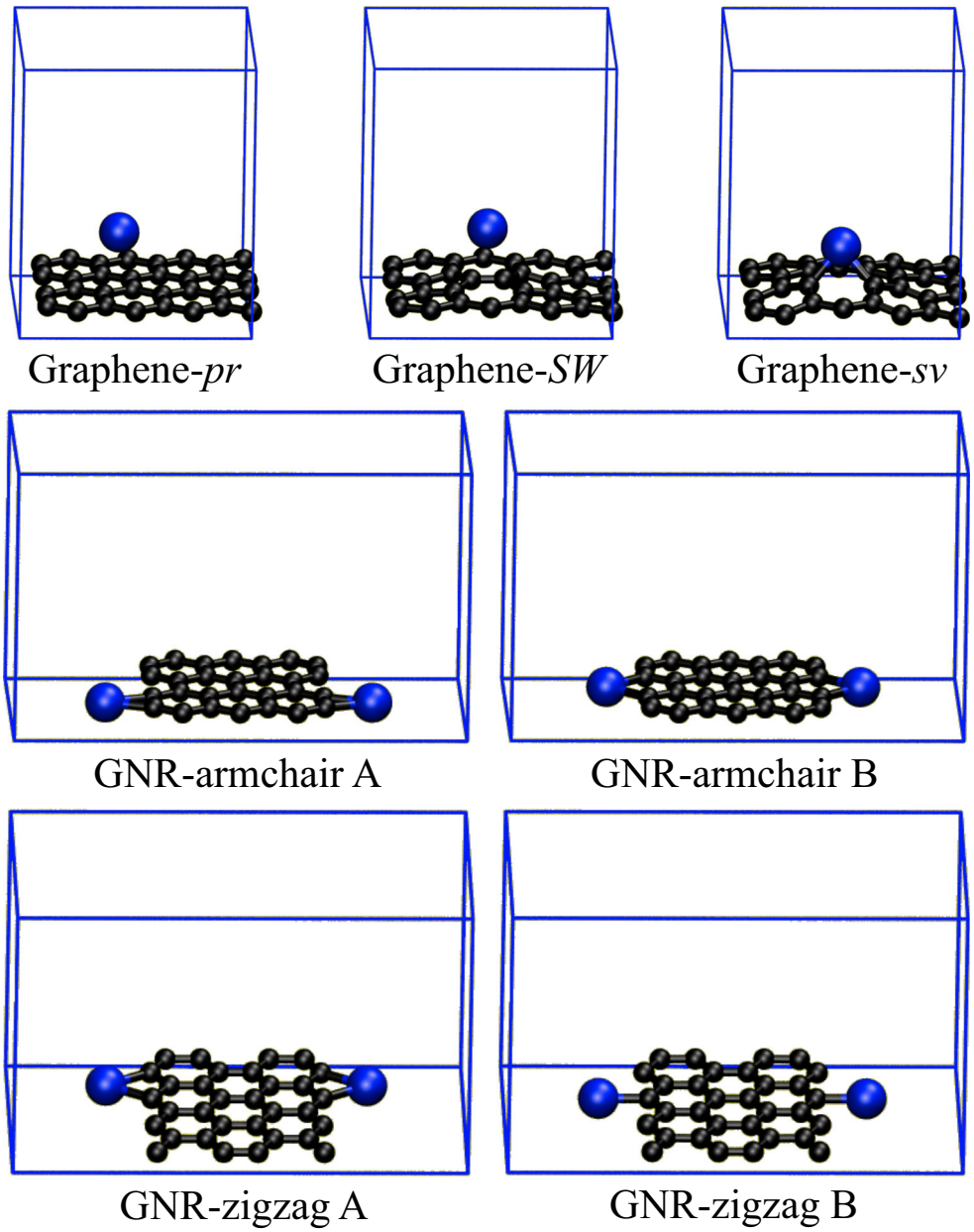

Fig. 9 Optimized adsorption structures for a Sn atom on the top of a pristine and defective graphene layer, as well as at the edge of a single graphene nanoribbon. C: black, Sn: blue

graphite. The diffusion coefficient of the samples was not obtained from EIS spectra because the diffusional response was not well defined for all the samples, showing some small instability at very low frequencies.

The double-layer capacitance of the electrodes was measured and was found to be similar for the three samples, with a value of approximately 1×10^{-5} F. Bearing in mind that the specific capacity of the double layer (c_e) is constant, with a value of 5×10^{-6} F/cm^2, and that the mass of the electrodes is 1 mg, then the area per unit of mass can be expressed as given by Eq. (5) [26]:

$$A_e = C c_e^{-1} m^{-1} \quad (5)$$

The resulting apparent diffusion coefficients and the data used are summarized in Table 1. As it can be seen, these coefficients are all in the order of 10^{-12} cm^2/s, which is in good agreement with other diffusion coefficients reported in the literature [27].

From the previous experimental results, it is possible to conclude that the nature of the carbonaceous support greatly affects the deposition of Sn nanoparticles. It is then possible to improve to a large extent the final electrochemical behavior of the electrodes by taking into account these aspects at the initial phase of the synthesis of an active material. When the carbon support is a disordered material with a high specific area, then the final metallic particles are smaller, well distributed, and

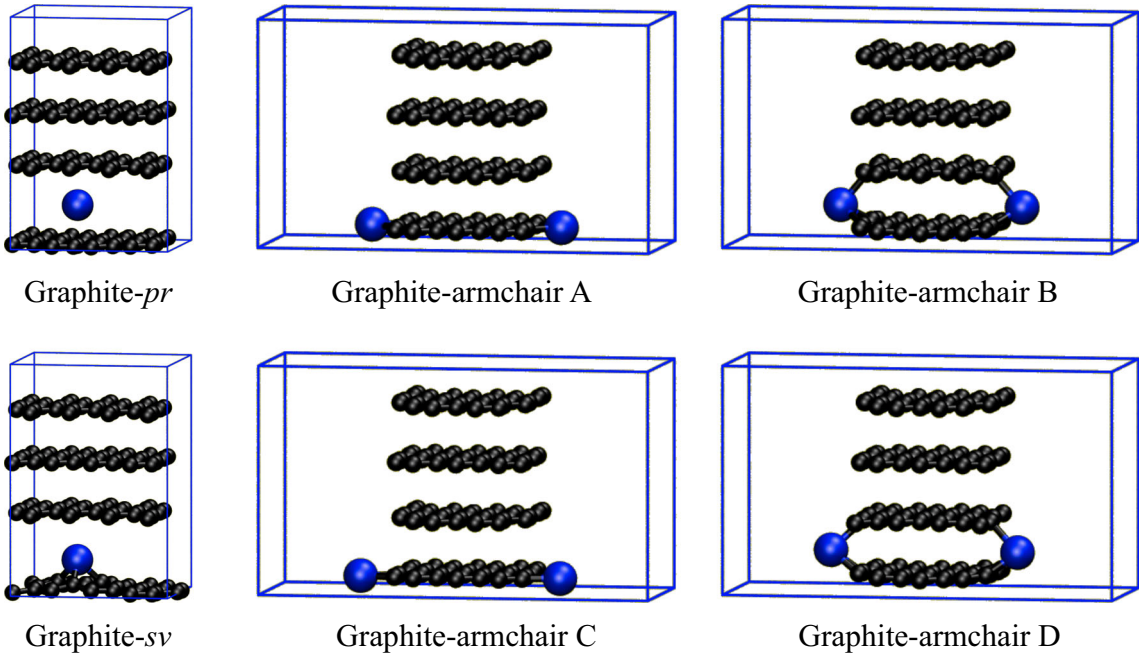

Fig. 10 Optimized adsorption structures for a Sn atom in pristine bulk graphite, in bulk graphite with a single vacancy, as well as on different positions at the edge of a stack of graphene nanoribbons. C: black, Sn: blue

with a better electrical contact from the point of view of the electrodes. This can be applied to improve the performance of batteries, where the electrochemical response is directly influenced by a good distribution of electrolytes and a large electroactive area. Thus, smaller particles are useful when the electrodes are used at high current densities in power battery applications. From the electrochemical results, it can then be inferred that electrode made from Sn nanoparticles supported on Super P® carbon (amorphous, electrical conductor, and relatively high surface area) has a superior performance in capacity and cycle life than the other carbon-based support materials evaluated in this study. This is particularly interesting due to the fact that amorphous carbon does not intercalate Li^+ ions by itself. Thus, the electrochemical response of the electrodes must be solely attributed to the adsorbed Sn nanoparticles.

DFT calculations

In order to rationalize the experimental findings, the three different carbonaceous materials were modeled by means of DFT calculations. The adsorption of a single Sn atom was simulated in different environments, to analyze the first step of the nucleation of Sn on the different carbonaceous structures.

Since the carbon nanotubes employed have a relatively large diameter (ca. 100 nm), the curvature at a ca. 15×15 $Å^2$ scale is negligible. Hence, adsorption of a single Sn on the surface of these carbon nanotubes can be modeled by a single graphene sheet. A pristine graphene surface (Graphene-*pr*) and the presence of defects such as a single carbon atom vacancy (Graphene-*sv*) were considered. Adsorption of Sn on the ends of the nanotubes was then modeled by graphene nanoribbons. Armchair (GNR-armchair) and zigzag (GNR-zigzag) edges were considered. Bulk graphite was modeled by explicitly considering a slab of four graphene layers with appropriate periodic boundary conditions. Adsorption of Sn between the layers of pristine graphite (Graphite-*pr*) and a defective material with a single carbon atom vacancy in one layer (Graphite-*sv*) was calculated. Graphite typically displays large flat terraces, as can be observed in Fig. 1b. Nonetheless, at the nanometric scale, the presence of steps becomes noticeable, see Fig. 2b. Adsorption of Sn in the vicinity of one of such steps was modeled using a stack of four graphene nanoribbons with periodic boundary conditions in the direction perpendicular to the graphene surface (Graphite-armchair). In this case, only the armchair edge was considered. The zigzag edge is ca. 1 eV per edge atom *less* stable than the armchair edge [28]. Finally, adsorption on disordered amorphous carbon structures was also studied to model the carbon Super P® employed in the experiments.

Adsorption energies, E_{ad}, obtained according to Eqs. (1) or (2) for the different structures are summarized in Table 2. The optimized geometries for all adsorbates are illustrated in Figs. 9, 10, and 11. As it can be observed, adsorption of Sn atoms is thermodynamically favorable with respect to the bulk material. This is due to the occurrence of carbon atoms with dangling bonds. Adsorption on the wall of large carbon nanotubes, such as those employed in the experiments, is largely disfavored by 2.76 eV as evidenced by the entry labeled as

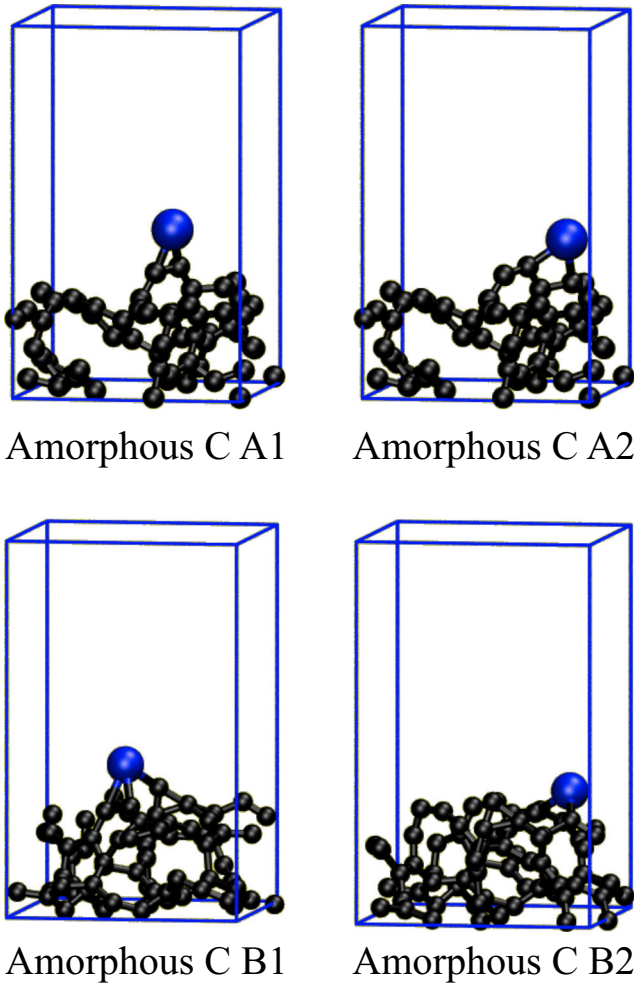

Fig. 11 Optimized adsorption structures for a Sn atom on two different amorphous carbon surfaces (A & B) and for two different adsorption sites (1 & 2) on each. C: black, Sn: blue

Graphene-*pr* in Table 2. Adsorption is expected to be favorable only at positions with an atom vacancy, or at the opened ends of the nanotubes.

Calculations also show that doping bulk graphite (Graphite-*pr*) with Sn atoms is strongly disfavored by ca. 4 eV. This result is consistent with the expansion of the carbon layers, neighboring to the Sn atom, in ca. 2.8 Å. This is consistent with the reduction of the van der Waals interactions between the carbon atoms. As in the case of the carbon nanotubes, adsorption of Sn is favorable at the edge of the material. Hence, nucleation of Sn should take place on the steps between large terraces of flat graphite.

The occurrence of such defects provides a higher density of defects on graphite in comparison with carbon nanotubes, where nucleation would start preferentially on the opened ends. This would explain the good experimental performance of graphite as compared to carbon nanotubes.

For the case of amorphous carbon, the calculations reported here show that adsorption sites present a wide range of E_{ad} values, from only mildly to largely favorable for adsorption. The higher density of favorable adsorption sites with respect to the other two carbonaceous materials is the most likely explanation for the better performance as anodic material for a Li-ion battery.

Bader charge analysis, reported in Table 2, reveals that a charge of 0.8–0.9 e is being transferred from the Sn atom to the carbon support material in all the cases in which a thermodynamically favorable adsorption process is observed. Although this is also the case for bulk graphite (labeled as Graphite-*pr* in Table 2), the large (ca. 2 Å) increment in the interplanar distance and the consequent decrease of van der Waals C–C interactions account for the largely unfavorable Sn adsorption. Such large charge transfer has also been observed in similar calculations reported for a Sn atom adsorbed on pristine and defective graphene sheets [29]. Projected Density of States (pDOS) analysis shows that there is a covalent interaction between Sn and C atoms in defective sites owed to a strong hybridization of C-2p with Sn-5s and Sn-5p orbitals. Taking into account that the Pauling electronegativity of C (2.55) is larger than that for Sn (1.96) [30], then it is reasonable to expect a larger electron density and, thus, a negative charge on the C atoms upon bond formation.

The energy values reported on Table 2 can be easily turned into the electrochemical scale. If the potential is referred to a Sn electrode in the same solution, say V_{Sn}, and entropy effects are neglected, then Eq. (6) holds,

$$V_{Sn} = -ze_0E_{ad} \tag{6}$$

where $z = 2$, e_0 is the electronic charge and V_{Sn} and E_{ad} are given in V and eV, respectively. Thus, the positive values of Table 2 correspond to *overpotential* Sn deposition, whereas negative ones correspond to *underpotential* deposition. Thus, we see that some sites on amorphous carbon may already be decorated under moderate reducing conditions, while Sn insertion into pristine graphite is completely out of question. The same can be stated for Sn deposition on pristine graphenic layers, where an overpotential of about 1.38 V can be predicted. Since the carbon nanotubes used here present a relatively large curvature radius, the situation for Sn deposition on their surface should be similar to that of graphene. Thus, we also conclude that Sn decoration on these nanostructures may only take place on defective sites of the nanotubes, or at least at their ends, as long as they are open or not saturated by other reactive species during their fabrication.

Conclusions

The reduction of $SnCl_2$ by $NaBH_4$ on three different carbonaceous substrates was studied, and their electrochemical behavior when used as negative electrodes for Li-ion batteries was

determined. Morphologically, it was found that smaller and more disperse particles are achieved when $SnCl_2$ is reduced on a defect-rich substrate, and that bigger clusters are formed on a more ordered substrate. In all cases, the capacities of the electrodes were higher than commercially used graphite. In terms of cyclability, the prepared electrodes show a good behavior for over 100 cycles. Of the three cases analyzed, the Sn-BH-SP sample had the highest capacity retention (67% after 100 cycles at a current of 1 C) and is therefore a very good candidate for further development. It is also noteworthy that the electrochemical response of the Sn-BH-SP sample is due mainly to the Sn nanoparticles dispersed on it, as the amorphous carbon is incapable of undergoing lithiation. The apparent lithium diffusion coefficients calculated for the samples were slightly lower than the diffusion coefficient for commercial graphite, implying that tin-based electrodes would be good candidates for anodes in high current density applications. Consistently with the experimental results, the first principles calculations show that amorphous carbon should be more easily decorated than the other carbonaceous structures. Furthermore, they predict that if large perfect, isolated, nanotubes or perfect graphite structures were used, these nanostructures could be only decorated under extreme reducing conditions, probably out of reach of current experimental conditions.

Acknowledgments This work was supported by PIO Conicet-YPF 3855/15, Y-TEC, Agencia Nacional de Promoción Científica, Program BID-Foncyt (PICT-2012-2324, PICT-2015-1605) Argentina, PID Conicet-11220110100992, PID Conicet-11220150100624, CONICET PUE "Desarrollo de baterías de litio" and SeCyT, from the National University of Cordoba. This work used computational resources from CCAD—Universidad Nacional de Córdoba (http://ccad.unc.edu.ar/), in particular the Mendieta Cluster, which is part of SNCAD—MinCyT, República Argentina.

References

1. Derrien G, Hassoun J, Panero S, Scrosati B (2007) Nanostructured Sn–C composite as an advanced anode material in high-performance lithium-ion batteries. Adv Mater 19(17):2336–2340. https://doi.org/10.1002/adma.200700748
2. Chen JS, Archer LA, Lou XW (2011) SnO2 hollow structures and TiO2 nanosheets for lithium-ion batteries. J Mater Chem 21(27): 9912–9924. https://doi.org/10.1039/c0jm04163g
3. Kamali AR, Fray DJ (2011) Tin-based materials as advanced anode materials for lithium ion batteries: a review. Rev Adv Mater Sci 27: 14–24
4. Wang Y, Lee JY, Deivaraj TC (2004) Tin nanoparticle loaded graphite anodes for Li-ion battery applications. J Electrochem Soc 151(11):A1804–A1809. https://doi.org/10.1149/1.1799491
5. Trifonova A, Wachtler M, Wagner MR et al (2004) Influence of the reductive preparation conditions on the morphology and on the electrochemical performance of Sn/SnSb. Solid State Ionics 168(1-2):51–59. https://doi.org/10.1016/j.ssi.2004.01.027
6. Yao J, Shen X, Wang B, Liu H, Wang G (2009) In situ chemical synthesis of SnO2–graphene nanocomposite as anode materials for lithium-ion batteries. Electrochem Commun 11(10):1849–1852. https://doi.org/10.1016/j.elecom.2009.07.035
7. Kim I-T, Lee J, An J-C et al (2016) Capacity improvement of tin-deposited on carbon-coated graphite anode for rechargeable lithium ion batteries. Int J Electrochem Sci 11:5807–5818
8. Chee S-S, Lee J-H (2012) Reduction synthesis of tin nanoparticles using various precursors and melting behavior. Electron Mater Lett 8(6):587–593. https://doi.org/10.1007/s13391-012-2086-y
9. Hsiao L-Y, Duh J-G (2006) Revealing the nucleation and growth mechanism of a novel solder developed from Sn-3.5 Ag-0.5 Cu nanoparticles by a chemical reduction method. J Electron Mater 35(9):1755–1760. https://doi.org/10.1007/s11664-006-0230-x
10. Egashira M, Takatsuji H, Okada S, Yamaki J (2002) Properties of containing Sn nanoparticles activated carbon fiber for a negative electrode in lithium batteries. J Power Sources 107(1):56–60. https://doi.org/10.1016/S0378-7753(01)00980-6
11. Yu P, Popov BN, Ritter JA, White RE (1999) Determination of the lithium ion diffusion coefficient in graphite. J Electrochem Soc 146(1):8–14. https://doi.org/10.1149/1.1391556
12. Wang Y, Zeng HC, Lee JY (2006) Highly reversible lithium storage in porous SnO2 nanotubes with coaxially grown carbon nanotube overlayers. Adv Mater 18(5):645–649. https://doi.org/10.1002/adma.200501883
13. Giannozzi P, Baroni S, Bonini N, Calandra M, Car R, Cavazzoni C, Ceresoli D, Chiarotti GL, Cococcioni M, Dabo I, Dal Corso A, de Gironcoli S, Fabris S, Fratesi G, Gebauer R, Gerstmann U, Gougoussis C, Kokalj A, Lazzeri M, Martin-Samos L, Marzari N, Mauri F, Mazzarello R, Paolini S, Pasquarello A, Paulatto L, Sbraccia C, Scandolo S, Sclauzero G, Seitsonen AP, Smogunov A, Umari P, Wentzcovitch RM (2009) QUANTUM ESPRESSO: a modular and open-source software project for quantum simulations of materials. J Phys Condens Matter 21(39):395502. https://doi.org/10.1088/0953-8984/21/39/395502
14. Perdew JP, Burke K, Ernzerhof M (1996) Generalized gradient approximation made simple. Phys Rev Lett 77(18):3865–3868. https://doi.org/10.1103/PhysRevLett.77.3865
15. Shao Y, Wang J, Engelhard M, Wang C, Lin Y (2010) Facile and controllable electrochemical reduction of graphene oxide and its applications. J Mater Chem 20(4):743–748. https://doi.org/10.1039/B917975E
16. Shin H-J, Kim KK, Benayad A, Yoon SM, Park HK, Jung IS, Jin MH, Jeong HK, Kim JM, Choi JY, Lee YH (2009) Efficient reduction of graphite oxide by sodium borohydride and its effect on electrical conductance. Adv Funct Mater 19(12):1987–1992. https://doi.org/10.1002/adfm.200900167
17. Monkhorst HJ, Pack JD (1976) Special points for Brillouin-zone integrations. Phys Rev B 13(12):5188–5192. https://doi.org/10.1103/PhysRevB.13.5188
18. Plimpton S (1995) Fast parallel algorithms for short-range molecular dynamics. J Comput Phys 117(1):1–19. https://doi.org/10.1006/jcph.1995.1039
19. Chenoweth K, van Duin ACT, Goddard WA (2008) ReaxFF reactive force field for molecular dynamics simulations of hydrocarbon oxidation. J Phys Chem A 112(5):1040–1053. https://doi.org/10.1021/jp709896w
20. Marks NA, Cooper NC, McKenzie DR, McCulloch DG, Bath P, Russo SP (2002) Comparison of density-functional, tight-binding, and empirical methods for the simulation of amorphous carbon. Phys Rev B 65(7):75411. https://doi.org/10.1103/PhysRevB.65.075411
21. Han J, Gao W, Zhu J, Meng S, Zheng W (2007) Density-functional theory study of the microstructure, electronic structure, and optical properties of amorphous carbon. Phys Rev B 75(15):155418. https://doi.org/10.1103/PhysRevB.75.155418
22. Auer E, Freund A, Pietsch J, Tacke T (1998) Carbons as supports for industrial precious metal catalysts. Appl Catal A Gen 173(2): 259–271. https://doi.org/10.1016/S0926-860X(98)00184-7

23. Zheng H, Jiang K, Abe T, Ogumi Z (2006) Electrochemical intercalation of lithium into a natural graphite anode in quaternary ammonium-based ionic liquid electrolytes. Carbon 44(2):203–210. https://doi.org/10.1016/j.carbon.2005.07.038
24. Ahn D, Xiao X (2011) Extended lithium titanate cycling potential window with near zero capacity loss. Electrochem Commun 13(8):796–799. https://doi.org/10.1016/j.elecom.2011.05.005
25. DYW Y, Fietzek C, Weydanz W et al (2007) Study of LiFePO4 by cyclic voltammetry. J Electrochem Soc 154:A253–A257
26. Robledo CB, Thomas JE, Luque G, Leiva EPM, Cámara O, Barraco D, Visintin A (2014) An experimental and theoretical approach on the effect of presence of oxygen in milled graphite as lithium storage material. Electrochim Acta 140:160–167. https://doi.org/10.1016/j.electacta.2014.05.117
27. Kim I, Blomgren GE, Kumta PN (2004) Sn/C composite anodes for Li-ion batteries. Electrochem Solid-State Lett 7(3):A44–A48. https://doi.org/10.1149/1.1643792
28. Okada S (2008) Energetics of nanoscale graphene ribbons: edge geometries and electronic structures. Phys Rev B 77(4):41408. https://doi.org/10.1103/PhysRevB.77.041408
29. Sun M, Peng Y (2014) Study on structural, electronic and magnetic properties of Sn atom adsorbed on defective graphene by first-principle calculations. Appl Surf Sci 307:158–164. https://doi.org/10.1016/j.apsusc.2014.04.005
30. Lide DR (1999) CRC handbook of chemistry and physics, 80th edn. CRC Press, Boca Raton